(Received 14 November 2024, Accepted 31 December 2024, Scheduled 14 February 2025)

Design and Analysis of a Delta-Shaped Segmented Variable Leakage Flux Reverse-Salient Permanent Magnet Synchronous Machine for Electric Vehicles

Xiping Liu, Jiao Guo, Ruipan Lu, Zhangqi Liu*, and Baoyu Sun

School of Electrical Engineering and Automation, Jiangxi University of Science and Technology, Ganzhou 341000, Jiangxi, China

ABSTRACT: Since the traditional Delta-shaped motor is difficult to achieve the wide speed range while increasing the output torque, it cannot fully meet the complex working conditions of electric vehicles. This paper, from the driving conditions and the principle of variable leakage magnetism, based on the traditional Delta-shaped interior motor, designs a variable leakage flux permanent magnet synchronous motor with a segmented Delta-shaped rotor permanent magnet structure (VLF-DSPM). The permanent magnet is segmented into a magnetic bridge by a ferromagnetic material so that some magnetic lines do not pass through the permanent magnet but directly through the magnetic bridge to increase the d-axis inductance. A magnetic barrier is designed in the q-axis to achieve magnetic leakage in the high-speed region, thereby achieving a wide speed control range. In addition, since the utilization rate of the permanent magnet is reduced due to segmentation, the output torque is reduced. Therefore, transverse bar-shaped permanent magnets are added to increase the reluctance torque of the motor to achieve a higher resultant torque. The key parameters of this structure were then optimized, and finally the electromagnetic characteristics of the VLF-DSPM were studied using finite element analysis in comparison with a conventional Delta-shaped interior permanent magnet (DS-IPM) synchronous motor. The results show that the VLF-DSPM has better flux control capabilities, higher output torque, a wider speed range, and higher efficiency and power factor.

1. INTRODUCTION

Electric vehicles (EVs) have rapidly evolved into a crucial component of the automotive industry, largely due to their notable advantages in terms of cleanliness and high efficiency. Its operating conditions are complex and variable, and in the face of increasingly complex traffic conditions such as frequent starting and stopping, acceleration and deceleration, hill climbing, and high-speed cruising, the results of many scholars' studies can be broadly categorized into the demand for high torque and high output at low speeds, and the demand for a weak magnetic wide speed regulation range at high speeds. However, permanent magnet synchronous motors (PMSMs), with their superior high efficiency and high-power factor, dominate today's electric vehicle industry. Since electric vehicles use permanent magnet synchronous motor drive (PMSM) as the mainstream drive technology, the performance of PMSM inside the vehicle will directly affect the overall performance of the electric vehicle [1–5]. Aiming to meet the diversified drive performance requirements of electric vehicles under complex operating conditions, many scholars have conducted continuous and in-depth research from different perspectives. Ref. [6] introduced the high magnetic energy product of rare-earth neodymium-iron-boron (NdFeB) permanent magnets into the design of synchronous reluctance motors and developed a permanent magnet-assisted reluctance motor with high torque density for vehicles, which combines the advantages of permanent magnets and reluctance motors. The German BMW i3 series also uses a double-layer permanent magnet rotor design, similar to the structure of synchronous reluctance motors, which improves the motor's power density, speed range, and output torque. However, its torque pulsation leads to higher noise and vibration. In addition, its production is affected by market supply and resource reserves due to the use of non-renewable resources, such as NdFeB, as permanent magnet materials [7–9]. In its four iterations, the Japanese Toyota PRIUS series of automobiles has extended the speed range from 5600 rpm to 17500 rpm, reducing the size by 33% and the mass by 12%, but excessive current density generates additional heat as well as larger weak magnetic currents, and the corresponding copper consumption in the windings may reduce the efficiency of the motor in the weakly magnetized control region and may lead to irreversible demagnetization phenomenon, which affects the long-term performance, especially under extreme conditions, and consequently the power factor and efficiency [10, 11].

For the above traditional interior permanent magnet synchronous motor structure, it is contradictory to improve the output torque and widen the range of constant power speed regulation. To overcome the problem that the air gap magnetic field is difficult to adjust, some scholars have proposed some motors with research significance in recent years. For example, the hybrid excitation motor with additional electric excitation [12, 13] can save the number of rare-earth materials and have high efficiency and flexible control. However, the extra excitation winding reduces the rotor space, decreases the torque output,

* Corresponding author: Zhangqi Liu (liuzhq@jxust.edu.cn).

and increases the copper consumption. Another kind of memory permanent magnet motor [14], which regulates the air-gap magnetic field by controlling pulses, can flexibly change and control the size of the air-gap flux of the motor through the online dynamic adjustment of the magnetizing winding current, but it increases the risk of demagnetization and torque pulsation, so the application scenarios have limitations. In fact, mechanical variable leakage motors change the motor excitation circuit through an external mechanical device to realize variable leakage, but they require high precision machining, resulting in high manufacturing cost and low feasibility [15]. In fact, the reverse convex pole synchronous motor also belongs to a kind of motor that regulates the magnetic field, as an innovative motor design, researchers have proposed various improved rotor structures. The U-type permanent magnet structure in [16] can make full use of the reluctance torque generated by the asymmetry of the rotor magnetic circuit, which can provide greater power and torque under the same volume, and the V-type permanent magnet structure in [17] can improve the power density, optimize the dynamic response, and enhance the reliability. At the same time both have higher requirements for material selection and manufacturing process. The Delta-type rotor permanent magnet structure in [18] can more effectively utilize the limited space inside the rotor to accommodate more permanent magnet materials, which in turn improves the overall power output capability of the motor to better resist the centrifugal force generated by high-speed operation, and at the same time reduces the risk of demagnetization due to the changes in the external environment, which ensures the stable operation of the motor under different operating conditions. In [19, 20], scholars proposed a controllable leakage permanent magnet motor (VLF-PMSM), based on the principle of "variable leakage", through the rotor leakage bridge and q-axis magnetic barrier design to control the degree of leakage saturation to indirectly regulate the magnetic field of the air gap, which can realize the variable flux characteristics of less leakage under heavy loads and more leakage under light loads. It has advantages with wide speed range, high efficiency, and high output torque, which is very consistent with the development direction of electric vehicle motors [21, 22].

In summary, a Delta-shaped rotor permanent magnet segmented structure of variable leakage reverse-salient motor (VLF-DSPM) is designed and optimized, and the values of d- and q-axis inductances will be varied to adapt to the complex working conditions of electric vehicles. A bread-shaped magnetic barrier is set in the q-axis to realize the variable leakage characteristics, but the output torque of the permanent magnet decreases while the loss increases when the speed range of the motor is relatively wide. So, in this paper, this point is considered in the design of the motors, and a bar magnet is added to the Delta shape, which helps to increase the reluctant torque and thus the synthesized torque. In addition, the winding of the motor proposed in this paper uses a double-layer fractional slot centralized winding, which also reduces the copper loss to some extent and makes it better match the performance requirements.

This paper has the following sections. Section 2 analyzes the core requirements for the performance of electric vehicles in the complex conditions of actual operation and the principle of variable leakage motors, while Section 3 focuses on the design of the motor structure, magnetic circuit analysis and optimization of important structural parameters. Section 4 takes the traditional Delta-shaped interior motor as a comparison motor and uses the finite element analysis method to analyze the electromagnetic characteristics of the motor designed in this paper. Finally, Section 5 concludes the paper.

2. EVS WORKING CONDITION ANALYSIS AND DESIGN PRINCIPLES

2.1. Multiple-Operating Conditions of EVs

To simulate and evaluate various working conditions in urban or suburban areas, most countries use UDDS (urban dynamometer driving schedule) as shown in Fig. 1. There are various operating conditions in UDDS. Mode I: Low speed or heavy load. It needs to have a strong load-bearing capacity. Mode II: Low speed or light load. In this case, high output torque and high efficiency are required. In addition, if the EV starts or stops frequently due to traffic signals and congestion, a high-efficiency drive motor is required to minimize losses. Mode III: High speed or heavy load. The vehicle that drives at motor speed is stabilized around the rated speed. Mode IV: High speed or light load. Usually, the need to type motor speed stabilizes 3–5 times of the constant power speed range, which needs to broaden the motor speed range. According to that the speed of low-speed area occupies 35%, and high-speed area occupies 65%, combined with the load requirements, mainly divided into low-speed heavy-duty and high-speed light-duty situation, low-speed heavy-duty to high torque and high efficiency, high-speed light-duty need a wide range of speed control and high output power, and maintain sufficient output torque.

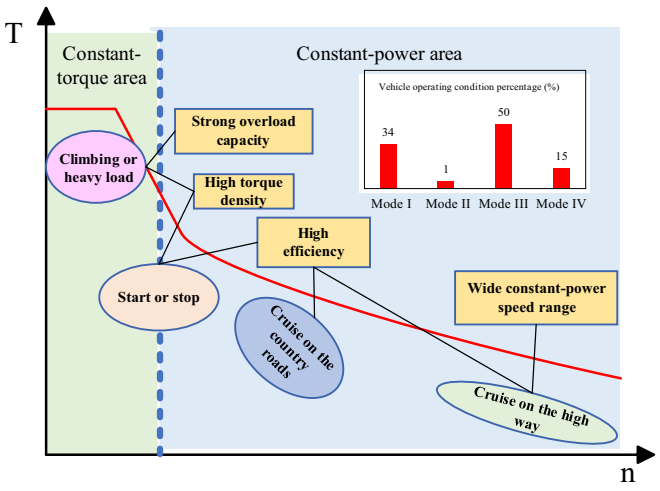

FIGURE 1. Multiple operating conditions.

2.2. Variable Leakage Flux Principle

EVs drive motors are required to be able to output the corresponding torque according to the size of the load, which is mainly realized by controlling the value of the d- and q-axis

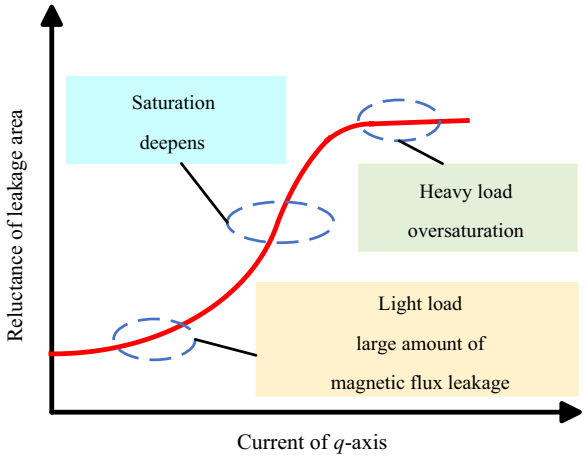

FIGURE 2. Variable leakage flux principle.

currents under different operating conditions to change the degree of saturation of the magnetic circuit, and the leakage magnetism variability can be explained by Fig. 2.

When the load is light, the q-axis current is very small, and the magnetic resistance of the leakage area is also very small, so a large amount of armature flux flows into the leakage area; the q-axis has only a small amount of flux; and the degree of saturation of the motor is very shallow currently. As the load increases, the q-axis current and leakage area reluctance gradually increase; the leakage flux decreases; and the saturation degree of the motor deepens; the leakage flux gradually decreases. When the load increases to a certain degree, the motor's q-axis current increases, and leakage magnetoresistance will tend to smooth out and reach the maximum value. Currently the motor is in a supersaturated state, and the leakage is very little.

For conventional IPM motors, ignoring the leakage magnetism and the degree of saturation of the motor, (1) is its air gap flux formula, and the air gap flux is equal to the sum of the armature flux and permanent magnet flux.

$$\Phi_\delta = \Phi_{pm0} + \Phi_a \tag{1}$$

where Φ_δ and Φ_a are the air gap flux and the flux generated by the armature, respectively. Φ_{pm0} is the total magnetic flux generated by the permanent magnets at no load, which is a constant. However, the effective air gap flux of a variable leakage motor due to the leakage flux path can be expressed as (2).

$$\Phi_\delta = (\Phi_{pm0} - \Phi_{\sigma 0}) + \Phi_a = \Phi_{pm0} + (\Phi_a - \Phi_{\sigma 0}) \tag{2}$$

$\Phi_{\sigma 0}$ is the no-load leakage flux, and the total leakage flux at load can be expressed as

$$\Phi_\sigma = \Phi_{\sigma 0} - \Phi_{\sigma a} \tag{3}$$

where $\Phi_{\sigma a}$ is the magnetic flux of the armature through the magnetic bridge at load, and since the reluctance of the leakage flux-conducting bridge is much smaller than that of the PMs, the flux of the bridge is much larger than that of the PMs, which is almost equal to the main flux of the armature windings, then

$$\Phi_\sigma = \Phi_{\sigma 0} - \Phi_a \tag{4}$$

$$\Phi_\delta = \Phi_{pm0} - \Phi_\sigma \tag{5}$$

Since Φ_{pm0} is a fixed constant, the effective flux of the variable leakage motor is only related to the total leakage flux, and the leakage flux is closely related to the size of the q-axis current. The q-axis current can change the size of the q-axis flux to achieve the purpose of controlling the degree of saturation of the leakage bridge to achieve the purpose of controlling the leakage of permanent magnets, and to realize the effect of the motor's "leakage variable".

3. MOTOR STRUCTURE, MAGNETIC CIRCUIT ANALYSIS AND PARAMETER OPTIMIZATION

3.1. Topology Design Process of VLF-DSPM

When the motor is in "low speed and heavy load" working condition, the decrease of variable reluctance helps to increase the effective magnetic flux, and the increase of effective magnetic flux can improve the output torque. When the motor is under "high speed and light load" condition, the effective flux decreases with the increase of variable reluctance, and the reduction of effective flux helps to widen the speed control range. Based on the design method of permanent magnet flux path segmentation guidance in the flux-variable region, a leakage-controllable, wide-speed-regulating permanent magnet motors with a magnetic barrier is proposed. The design idea follows the flowchart in Fig. 3.

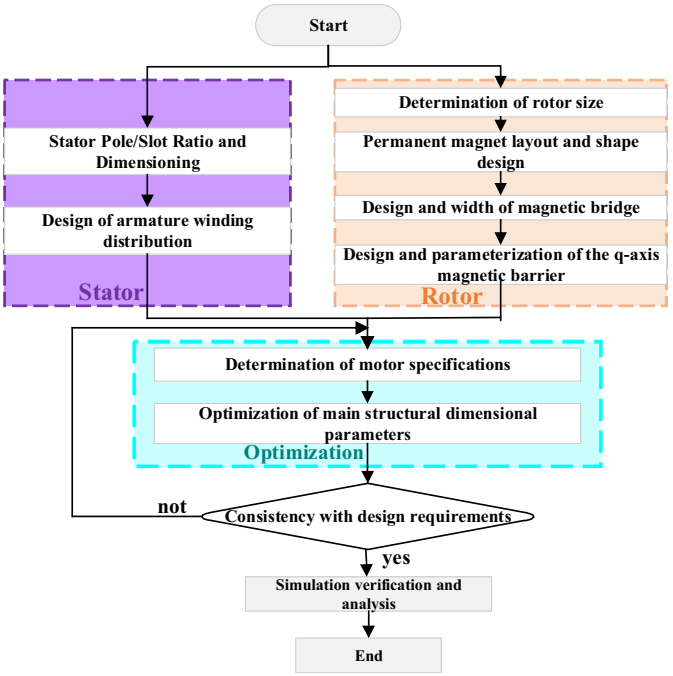

FIGURE 3. Design flowchart of VLF-PMSM.

By installing a Delta-type segmented permanent magnet with a leakage bypass feature and a magnetic barrier on the rotor side, the permanent magnet segmented variable leakage anti-convex pole motor realizes a larger range of flux variation. The design idea and its segmented evolution process are shown in Fig. 4.

3.2. VLF-DSPM Motor Topology

The topology of the motor is shown in Fig. 5(a), the leakage region shown in (b), and the main optimization parameters shown

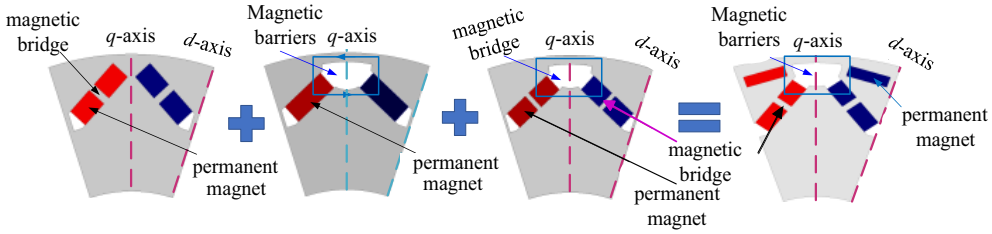

FIGURE 4. Rotor segmentation design process for VLF-DSPM.

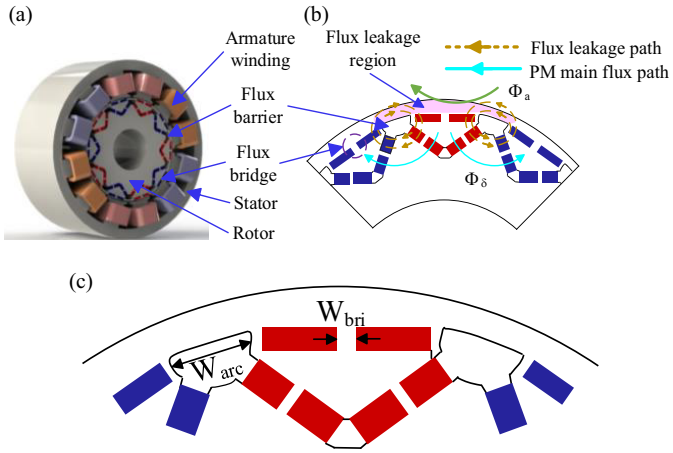

FIGURE 5. VLF-DSPM machine. (a) Topology. (b) Flux leakage region. (c) Design parameters configuration.

in (c). A double-layer fractional-slot centralized winding is used, with 10-pole and 12-slot pole-slot ratios, and a built-in rotor structure, with five pairs of permanent magnets embedded in the rotor, alternately in a Delta-shaped arrangement. To further increase the weak-magnet capability of the motor, the permanent magnets are segmented, and the magnetic bridges are formed between the two segments of the permanent magnets to increase the inductance of the d-axis. Correspondingly, a bread-shaped magnetic barrier is placed along the q-axis of the permanent magnet so that most of the q-axis flux flows through the magnetic bridge. In addition, an air magnetic barrier is also provided at the end of the permanent magnet, whose main purpose is to allow the leakage magnetism in the magnetic bridge to form a crosslink with the q-axis armature flux, so that the leakage magnetism can be more easily controlled by the q-axis armature magnetomotive force, in order to realize the effect of variable leakage magnetism. In addition, the design of the bar-shaped permanent magnet is favorable to reduce the d-axis inductance to increase the synthesized torque.

3.3. Magnetic Circuit Analysis under Various Conditions

The magnetic circuits of the controllable leakage motor proposed in this paper are also different under different operating conditions, Figs. 6(a), (b) and (c), (d) show the d- and q-axis equivalent magnetic circuits for high-speed operating conditions, and the d- and q-axis equivalent magnetic circuits for low-speed operating conditions, respectively.

From Figure 6, it can be seen that at high speeds there is a large amount of leakage near the rotor magnetic barrier. The

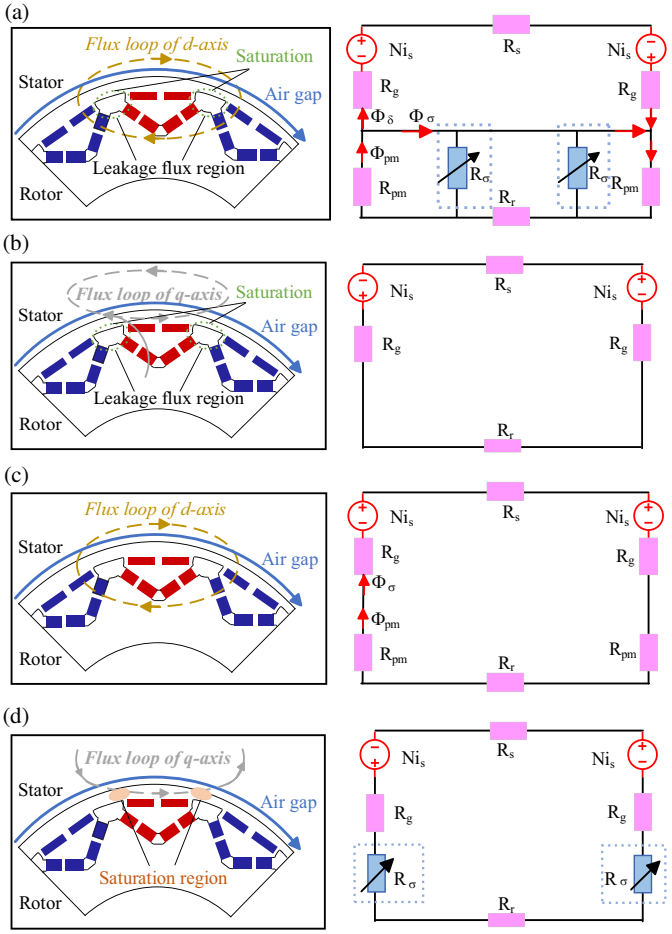

FIGURE 6. Equivalent magnetic circuit. (a) d-axis magnetic circuit at high speed. (b) q-axis magnetic circuit at high speed. (c) d-axis magnetic circuit at low speed. (d) q-axis magnetic circuit at low speed.

PM main flux is divided into the air gap flux that flows through the air gap and the leakage flux that passes through the leakage region at the periphery of the magnetic barrier, and there are two leakage loops in the equivalent magnetic circuit of the d-axis. Then there are the following equations.

$$\Phi_\delta(i_d, i_q) = \frac{2Ni_s}{2R_g + R_s + R_r + 2\xi R_{pm}} \tag{6}$$

$$\xi = \frac{R_\sigma(i_d, i_q)}{R_{pm} + R_\sigma(i_d, i_q)} \tag{7}$$

where N is the number of armature winding turns; R_{pm}, R_s, R_r, R_g, and $R_\sigma(i_d, i_q)$ represent PM reluctance, stator core re-

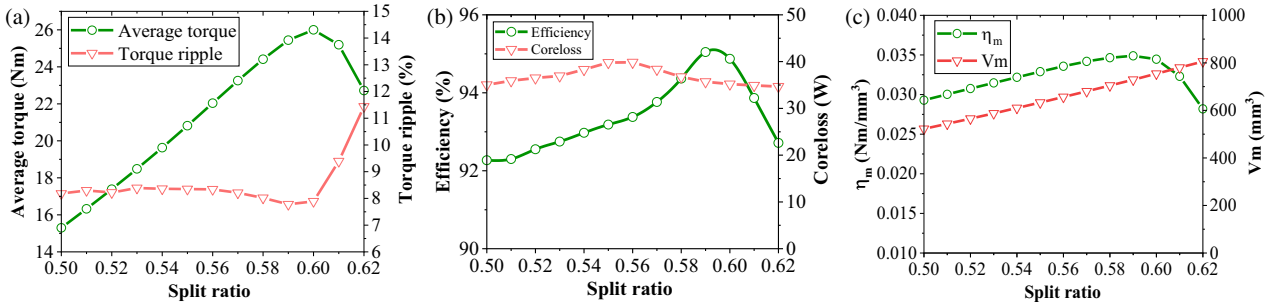

FIGURE 7. Variations of average torque, torque ripple, efficiency, core loss, PM utilization ratio and volume with split ratio in VLF-DSPM. (a) Average torque and torque ripple. (b) Efficiency and core loss. (c) PM utilization ratio and volume V_m.

luctance, rotor core reluctance, air gap reluctance, and magnetic bridge reluctance, respectively. Since ξ is always a constant less than 1, the permanent magnet field is easier to regulate, and R_σ in parallel with R_{pm} results in a parallel reluctance ξR_{pm} less than R_{pm}. As a result, it increases, and the motor acquires an inverted-convex characteristic, which is favorable for extending the constant power speed range.

At low speeds,

$$\Phi_\delta(i_d, i_q) = \frac{2Ni_s}{2R_g + R_s + R_r + 2R\sigma(i_d, i_q)} \tag{8}$$

As the q-axis current increases, the q-axis PM flux component increases, resulting in a concentration of magnetic leakage. When the q-axis current increases to a certain extent, there are multiple saturation points in the magnetic circuit, and R_σ increases, resulting in the magnetic leakage to be almost 0, which increases the main flux, and the motor obtains a positively convex polarity characteristic, thus increasing the output torque.

3.4. Optimization of Main Design Parameters

Modification of the main stator and rotor parameters will have some effect on the electromagnetic performance of the VLF-DSPM motor, mainly including average torque, torque fluctuation, PM utilization, core loss, and efficiency.

3.4.1. Optimization of Important Stator Parameters

Aiming to obtain the optimum parameter ratios for motor performance, the stator parameter splitting ratio to be optimized is defined as (9).

$$\varepsilon_s = \frac{R_i}{R_o} \tag{9}$$

where R_i and R_o represent the inner and outer radii of the stator, respectively. Split ratio is one of the most representative parameters in the stator parameters of the motor, which is of great significance in improving the overall performance of the motor. The variation of average torque and torque pulsation, iron loss, and efficiency as well as permanent magnet volume and utilization of the motor with respect to the stator structure parameter, split ratio, obtained by means of finite element analysis is shown in Fig. 7.

In Fig. 7(a), the average torque is maximum, and the torque pulsation is minimum at the split ratio equal to 0.6. The average torque decreases slightly, and the torque ripple increases slightly at the split ratio of 0.59. In Fig. 7(b), the highest efficiency and the lowest iron loss is at the split ratio equal to 0.59, and the efficiency decreases slightly at the split ratio of 0.6. In Fig. 7(c) the point of the highest utilization of permanent magnets is at the split ratio equal to 0.59, and it starts to decrease sharply at the split ratio equal to 0.6. To sum up, the optimum value of the splitting ratio is 0.59.

3.4.2. Optimization of Important Rotor Parameters

The main parameters of the motor rotor optimization are shown in Fig. 5(c), where W_{arc} and W_{bri} are the width of the magnetic barrier and the width of the magnetic bridge. The variation of average torque, torque ripple, core loss and efficiency with rotor structural parameters W_{arc}, W_{bri} is obtained by using finite element analysis as shown in Fig. 8, where (a) and (b) show that in VLF-DSPM, with the increase of W_{bri}, the average torque increases significantly while the torque ripple is not significant, and the increase of A does not affect the average torque significantly but makes the torque ripple larger. In Figs. 8(c) and (d), it can be clearly seen that the changes of W_{bri} and W_{arc} affect the core loss and efficiency of the motor at the same time. When W_{bri} increases, the core loss of the motor increases, and efficiency does not change much. When W_{arc} increases, the core loss of the motor decreases significantly, but the reduced efficiency shows a tendency of increasing first and then decreasing.

In summary, the torque ripple in this motor is insensitive to the variation of the parameters of W_{arc} and W_{bri}, and a higher average torque of larger torque, smaller losses, and higher efficiency can be obtained when the value of W_{bri} is between 0.6 and 1.0, and the value of W_{arc} is between 3 and 5. Setting up magnetic bridges and barriers with appropriate widths can improve the situation of magnetic flux imbalance, which is conducive to increasing the torque while reducing the torque ripple, reducing the core losses, and improving the motor efficiency.

4. ELECTROMAGNETIC CHARACTERISTIC

Aiming to verify that the VLF-DSPM has good performance and to further analyze the advantages of this segmented Delta-

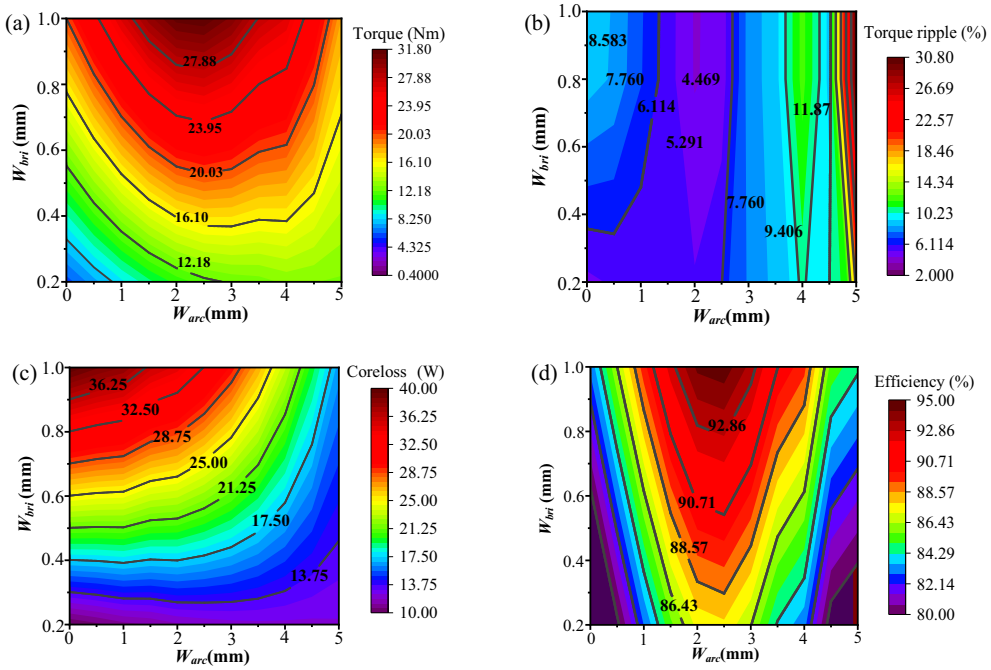

FIGURE 8. Variations of average torque, torque ripple, core loss and efficiency with flux barriers in VLF-DSPM. (a) Average torque. (b) Torque ripple. (c) Core loss. (d) Efficiency.

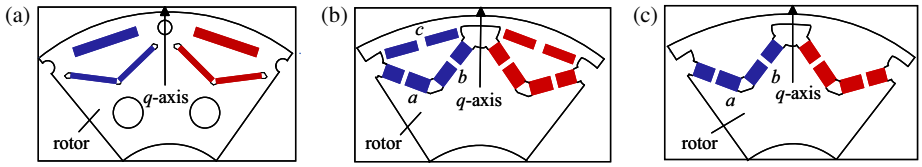

FIGURE 9. Rotor structure of the machine. (a) Conventional DS-IPM. (b) VLF-DSPM. (c) Removing the bar-shaped permanent magnet c of VLF-DSPM.

TABLE 1. Main dimensions and parameters of VLF-DSPM and DS-IPM.

Items	VLF-DSPM	DS-IPM
Rated output power (kW)	4	4
Current (A)	10	10
Air-gap length (mm)	0.7	0.7
Rated speed (rpm)	1500	1500
PM material	N42SH	N42SH
Stator and rotor core materials	DW310_35	DW310_35
Out diameter of the stator (mm)	155	155
Out diameter of the rotor (mm)	89.2	89.2
Slots/Poles	12/10	12/10
PM volume (mm^3)	696.4	667.6
Turns	20	20

shaped rotor permanent magnet, a conventional Delta-shaped interior permanent magnet synchronous motor (DS-IPM) with identical stator structure, pole-slot ratios, and almost equal number of permanent magnets is selected for comparison in this paper. The rotor structure of DS-IPM is shown in Fig. 9(a), and that of the VLF-DSPM motor is shown in Fig. 9(b). The structure in the main parameters and material configurations of VLF-DSPM and DS-IPM are shown in Table 1. They have the same stator structure parameters, and the permanent magnet volume of the optimized VLF-DSPM is slightly larger than that of the DS-IPM motor, which makes it fair to carry out the analysis of electromagnetic characteristics. Fig. 9(b) shows the rotor structure, and the structure after removing the bar permanent magnet c is shown in Fig. 9(c).

The electromagnetic characteristics of the two machines are analyzed under no load and load using finite element analysis to verify the good characteristics of the motor proposed in this paper, to prove the validity of the motor design, to analyze the advantages and disadvantages, and also to analyze the feasibility of the motor.

4.1. No-Load Characteristics

The magnetic cloud densities of VLF-DSPM and DS-IPM are obtained by using the method of finite element analysis as shown in Fig. 10. The variation of air gap flux density and back-electromotive force (back EMF) of VLF-DSPM and DS-IPM with the rotor position angle is shown in Fig. 11 and Fig. 12.

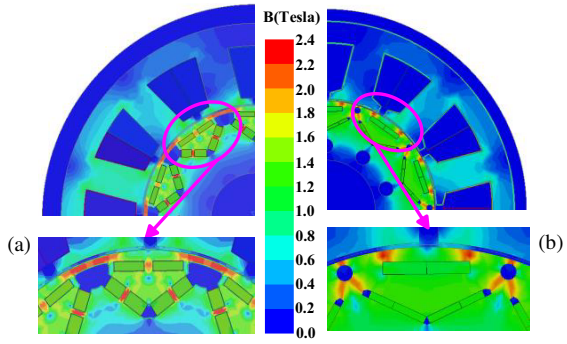

FIGURE 10. No-load magnetic flux distribution. (a) VLF-DSPM. (b) DS-IPM.

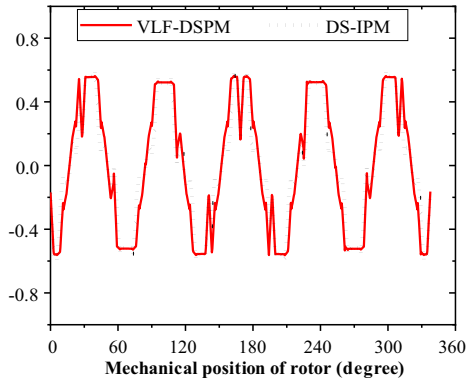

FIGURE 11. Variation of air gap flux density with rotor position.

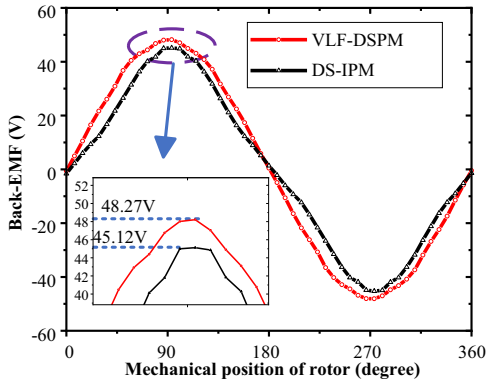

FIGURE 12. Variation of Back-EMF with rotor position.

The harmonic analysis of air gap magnetic density and back electromotive force in Fig. 11 and Fig. 12 are shown in Fig. 13 and Fig. 14, respectively. It can be clearly seen that, similar to the traditional Delta-shaped IPM, the VLF-DSPM motor has a 5-pair magnetic field distribution; the air-gap flux density and magnetic field density in the magnetic bridge under no-load situation show regular changes; the maximum magnitude of the magnetic field in the air-gap flux density is slightly higher than that in the DS-IPM motor; and the waveforms are smoother, which means that the weak electromagnetic capability has increased. The amplitude of the no-load back electromotive force of the VLF-DSPM motor is increased by 3.15 V, which means that the motor output capability and efficiency are also higher. The results of harmonic analysis of the waveforms in Figs. 11 and 12 are shown in Figs. 13 and 14. It is revealed that the first harmonic content of the air-gap flux density and the back electromotive force of the VLF-DSPM motor are higher than that of the DS-IPM motor, and the THD values of the air-gap flux density are 10.0% in VLF-DSPM and 23.1% in DS-IPM, respectively. The THD values of the back electromotive force are 1.78% in VLF-DSPM and 11% in DS-IPM respectively, which indicates that the high-frequency harmonic content of VLF-DSPM motor is greatly reduced, so it has lower core losses and a stronger output capacity.

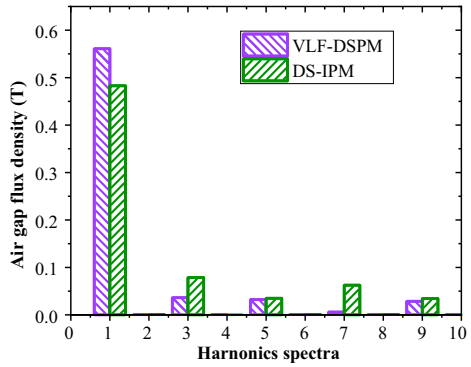

FIGURE 13. Harmonic analysis of the air gap flux density.

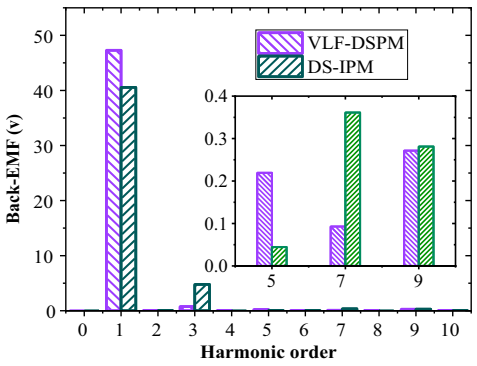

FIGURE 14. Harmonic analysis of the back-EMFs.

4.2. Electromagnetic Torque

From the analysis in Section 3, the d- and q-axis inductance values of the variable leakage motor are affected by its current value to varying degrees, and its torque equations in the d and q rotating coordinate system are (10)–(12)

$$T_{pm} = \frac{3}{2}P_n\psi_{pm}i_q \tag{10}$$

$$T_{rel} = \frac{3}{2}P_n i_d i_q(L_d - L_q) = \frac{3}{2}P_n L_d(1-\rho)i_d i_q \tag{11}$$

$$T_e = T_{pm} + T_{rel} \tag{12}$$

$$\rho = L_q/L_d \tag{13}$$

where P_n is the number of pole pairs of the motor, ψ_{pm} the permanent magnet flux, T_{pm} the permanent magnet torque, ρ the saliency ratio, and T_{rel} the reluctance torque. From (10)–(12), the synthesized torque of the motor can be divided into two parts, the permanent magnet torque and reluctance torque.

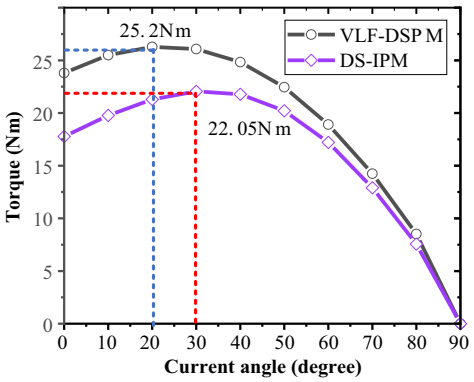

FIGURE 15. Variation of permanent magnet torque with current angle in VLF-DSPM and DS-IPM.

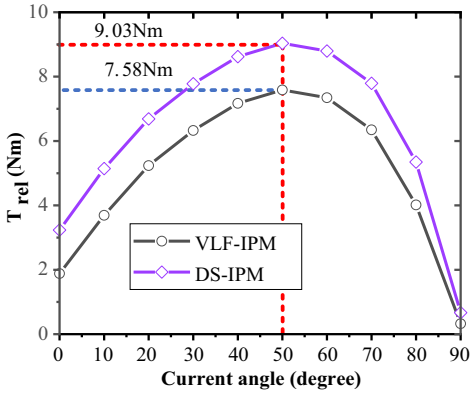

FIGURE 16. Variation of reluctance torque with current angle in VLF-DSPM and DS-IPM.

When the reluctance torque is greater than 0, the electromagnetic torque is increased, and the motor is in the driving or load state; when the saliency ratio of the motor is equal to 1, all the torque is converted into the electromagnetic torque, and the reluctance torque is 0; when the reluctance torque is negative, the electromagnetic torque is reduced, and the motor is in the braking state is 0; when the reluctance torque is negative, the electromagnetic torque is reduced, and the motor is in the braking state. Figs. 15 and 16 show the relationship curves between the electromagnetic torque and reluctance torque for the two motors at different current angles.

As can be seen from the figure, the VLF-DSPM motor has a higher electromagnetic torque due to its stronger magnetic tuning capability, and therefore a higher maximum torque increase of 3.15 Nm than the conventional Delta-shaped motor. The average value of the reluctance torque of the DS-IPM is 1.03 Nm higher than that of the VLF-DSPM because the former has a larger positive d-axis current, and the latter has a smaller negative d-axis current. In addition, as shown in Fig. 17, the electromagnetic torque of the VLF-DSPM motor is improved by 2.74 Nm compared to the motor with the permanent magnet c with the bar removed, and the reluctance torque content is higher. The c in the Delta-shaped permanent magnet facilitates the increase of the reluctance torque and thus the synthesized torque, which at the same time is in accordance with the previously mentioned point of view. The maximum content of the reluctance torque in the DS-IPM indicates that the content of the permanent magnet torque is low.

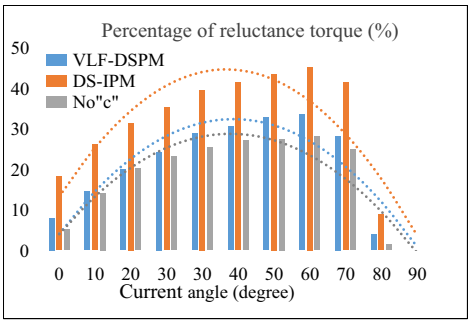

FIGURE 17. Percentages of reluctance torque in VLF-DSPM, DS-IPM and No "c" machine.

4.3. Overload Capacity

Figure 18 shows the change in the relationship between the ratio of the electromagnetic torque to the rated torque for the VLF-DSPM and DS-IPM with 1–2 times of the rated load. The abscissa i/i_N indicates the ratio of the load current to the rated current, and the ordinate T_e/T_N indicates the ratio of the electromagnetic torque to the rated torque under the corresponding load current. In Fig. 18, when the rated load current is applied, $i/i_N = 1$, the electromagnetic torque is $T = T_N$. When $i/i_N = 2$ (corresponding to EVs heavy load or climbing), the torque of the VLF-DSPM motor is only $1.81T_N$, while the torque of the DS-IPM motor reaches $1.96T_N$, proving that adding magnetic barriers can make the iron core less susceptible to saturation, thereby obtaining stronger overload capacity than the DS-IPM motor.

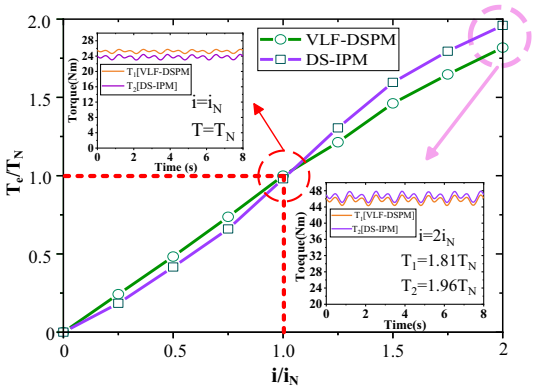

FIGURE 18. Electromagnetic torque versus current curve.

4.4. Inductance Characteristic

The changes of d-axis and q-axis inductances with the magnitude of current for the two motors can be visualized in Fig. 19. The VLF-DSPM motors basically satisfy the reverse-salient characteristic that L_d (d-axis inductance) is larger than L_q (q-axis inductance) at rated operating conditions, and the reverse-salient characteristic is more obvious. Due to the existence of the q-axis magnetic barrier, the leakage effect is good, and the decreasing speed of the d-axis inductance is obviously smaller than that of the q-axis inductance. However, the change of d-

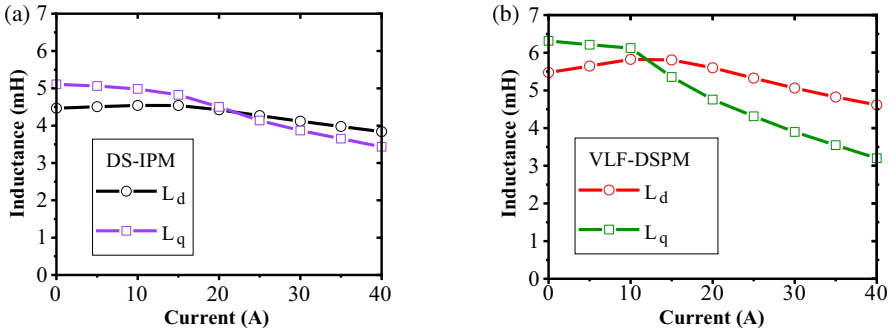

FIGURE 19. Variation of d-axis and q-axis inductances with current. (a) DS-IPM. (b) VLF-DSPM.

axis and q-axis inductances of DS-IPM motor is not significant, and the saliency ratio is close to 1. Obviously, the d-axis inductance of VLF-DSPM is larger, because the motor adopts ferromagnetic material to segment the Delta-shaped permanent magnets. The permeability of ferromagnetic material is much larger than that of permanent magnets, and a part of the magnetic lines of flux does not pass through the permanent magnets but directly passes through the ferromagnetic material, which makes the magnetic flux path of the main magnetic circuit longer and the magnetoresistance of the main magnetic circuit smaller, and thus makes the d-axis inductance larger and the range of constant-power speed regulation broader. Therefore, the proposed motor has a better weak magnetic effect.

4.5. Variable Leakage Flux Characteristic

The effective magnetic flux map of the VLF-DSPM obtained using the finite element analysis method is shown in Fig. 18. When the EVs are operated at the high speed and light load conditions shown in Fig. 20, the effective flux is small due to the presence of a magnetic barrier on the q-axis and a large amount of leakage flux near the barrier and around the bridge, and the effective flux is limited by the voltage-limit ellipse and the current-limit circle. The effective magnetic flux of the motor is limited to between 0.03 and 0.06 Wb. The motor can adjust the magnetic field through magnetic leakage. It is also clear from the magnetic flux line diagram in Fig. 21 that during high-speed light-load operation, there is more magnetic leakage near the magnetic barrier, and the motor is operating in the constant speed region. When the EVs are at low speed and heavy load,

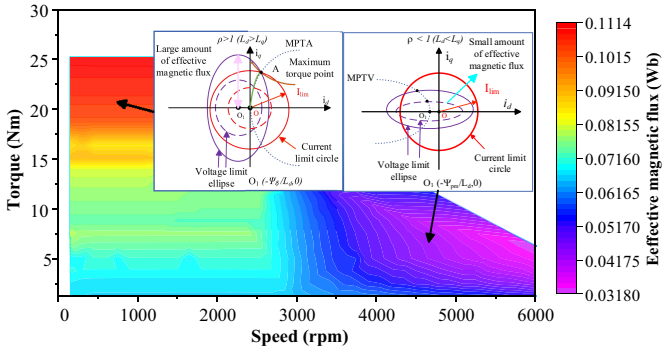

FIGURE 20. Effective flux map of VLF-DSPM motor.

there is a magnetic leakage saturation region in the motor, with very little magnetic leakage and an effective magnetic flux between 0.09 and 0.11 Wb. A large number of magnetic flux lines pass through the air gap, and the convex pole ratio $\rho < 1$ at this time, so a high torque can be output to meet the demand.

4.6. Constant-Power Speed Range (CPSR)

The CPSR performance of motors is crucial for EVs, and the torque-speed and power-speed curves of two motors are obtained at rated voltage and rated current as shown in Fig. 22. Thanks to the design of the q-axis magnetic barrier and segmented magnetic bridge, the flux regulation capability of the VLF-DSPM motor is increased, and the output torque of the proposed motor is higher than that of the DS-IPM motor in the low-speed region. The power of DS-IPM reaches its maximum value near the rated operating point and starts to decrease sharply near the speed of 4000 rpm, whereas the VLF-DSPM motor can maintain a higher output power in the constant power region until the speed rises to 6000 rpm, and then it reduces to the rated power, with a constant power speed range of up to four times of the rated speed. According to Fig. 22, when the output torque is 6.31 Nm, the maximum speed of DS-IPM motor is only 4350 rpm, while the maximum speed of VLF-DSPM motor is up to 6000 rpm, due to the stronger weak magnetic regulation capability of VLF-DSPM motor.

4.7. Efficiency and Power Factor

Efficiency is an important indicator of permanent magnet synchronous motors, and motors used in electric vehicles will receive greater attention, as efficiency is related to the motor's energy conversion rate and cost of use. Under the conditions of a phase current of 10 A and a DC voltage of 125 V, the efficiency diagrams of the two motors are shown in Fig. 23. From the picture, the efficiency of the VLF-DSPM motor is about 92% when it is near the rated operating point, while the efficiency of the DS-IPM motor is below 90% near the rated operating point. As the motor speed increases, the efficiency of the two gradually increases, and the maximum efficiency can reach 96% near the speed of 2000 rpm, but after the speed is higher than 4000 rpm, the efficiency of the former decreases slowly, between 92% and 95%, and after the speed is higher than 4000 rpm, the efficiency of the latter decreases quickly. It will be even lower than 88%.

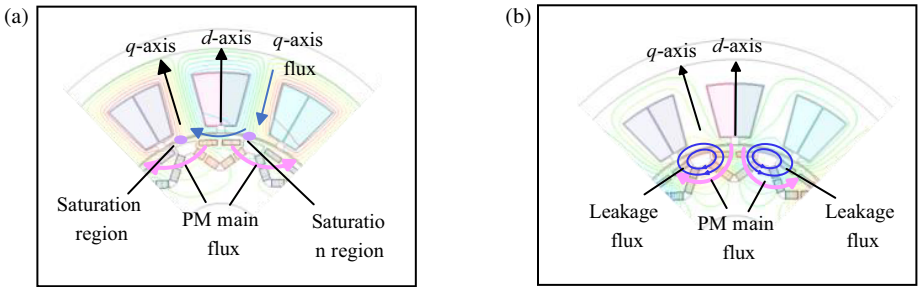

FIGURE 21. Magnetic lines of flux in VLF-DSPM motor under deferent condition. (a) Low speed and heavy load. (b) High speed and light load.

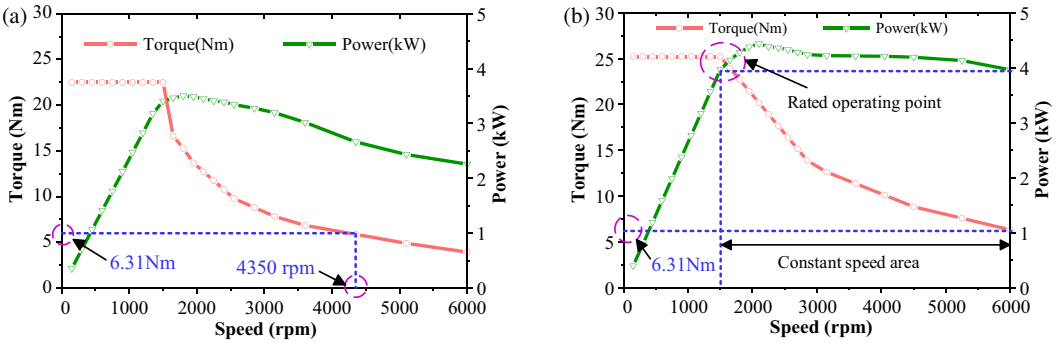

FIGURE 22. Torque-speed and power-speed curves. (a) DS-IPM. (b) VLF-DSPM.

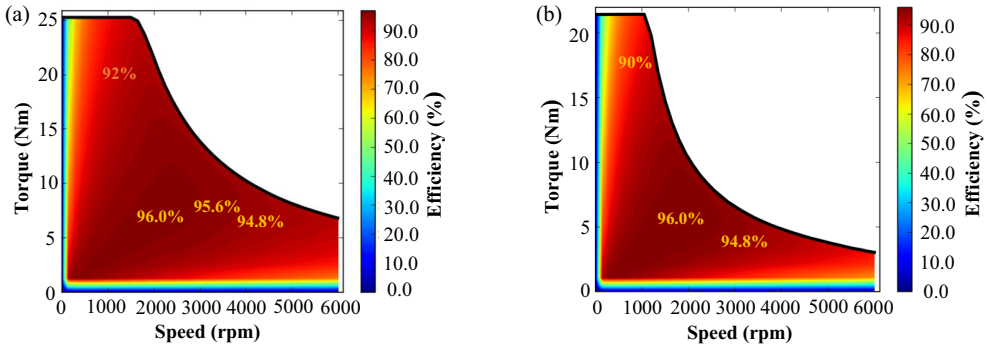

FIGURE 23. Efficiency maps of VLF-DSPM and DS-IPM. (a) VLF-DSPM. (b) DS-IPM.

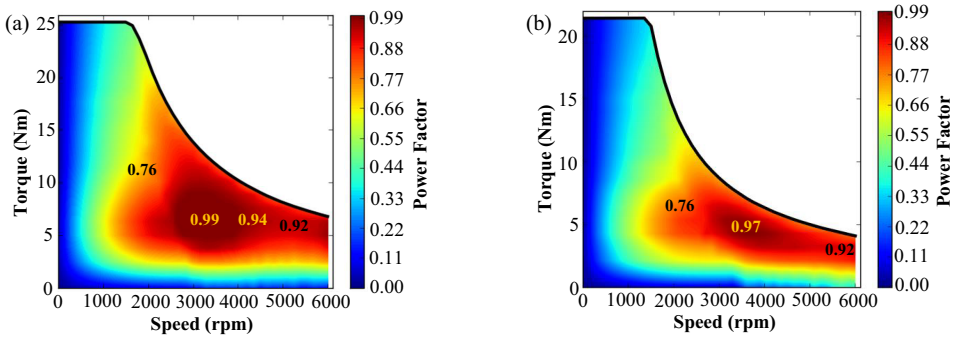

FIGURE 24. Power factor maps of VLF-DSPM and DS-IPM. (a) VLF-DSPM. (b) DS-IPM.

This proves that the former is more efficient and more advantageous in low-speed driving and high-speed sailing when the two have comparable maximum efficiencies.

Power factor is another important index to measure the performance of the motor, which reflects the degree of effective utilization of electrical energy during operation. The power factor maps of the VLF-DSPM and DS-IPM motors are shown

TABLE 2. Comparison results of the two machines.

Model	DS-IPM	Optimized VLF-DSPM
Air-gap density (T)	0.59	0.56
No load back-EMF (V)	45.12	48.27
Harmonic THD value of air-gap density (%)	23.1	10.0
Harmonic THD value of back-EMF (%)	11	1.78
Average torque (Nm)	22.05	25.2
Reluctance torque (Nm)	9.03	7.58
Split ratio	0.61	0.59
L_d/L_q	0.88	1.2
Efficiency (%)	95%	96%
Power factor	0.97	0.99
CPSR	2.9	4

in Figs. 24(a) and (b), respectively. It can be visualized that both have power factors lower than 0.76 near the rated operating point, but after higher than the rated rotational speed, the power factor of the former soars all the way up to 0.99, which can be maintained, while that of the latter in the high-speed region reaches 0.97 in a very small range. This is because the d-axis inductance of the proposed motor is increased after the optimized design of the rotor structure, which can solve the problem of low power factor of conventional motors in the high-speed travel domain.

5. CONCLUSION

Due to the insufficient output torque at high speeds of traditional Delta-shaped motors, their power factor and efficiency are low. While improving the output torque, it is difficult to maintain a wide speed regulation range, which cannot fully meet the reasonable requirements of the internal drive motor of electric vehicles operating under complex working conditions. Therefore, after many relevant papers are reviewed, this paper proposes a new segmented permanent magnet synchronous motor with variable flux leakage reverse salient characteristics based on the traditional Delta-shaped interior PMSM.

First, a simplified analysis of the magnetic circuit principle and the cause of the flux leakage of this motor was carried out through formula derivation.

Second, the stator split ratio of this motor was optimized, as well as the width parameters of the rotor magnetic barriers and magnetic bridges. The optimization targets were average torque, torque ripple, efficiency, core loss, and permanent magnet utilization. The optimal split ratio was found to be 0.59, and the optimal width ranges of the magnetic barriers and magnetic bridges were found to be between 3 and 5 mm, and 0.6 and 1 mm, respectively.

Finally, the DS-IPM motor with an identical stator structure and a similar number of permanent magnets to the motor mentioned in this article was compared to study the no-load characteristics, output torque, overload capacity, inductance characteristics, flux regulation characteristics, constant power speed range, efficiency, and power factor. It was found that the output torque of the motor mentioned in this article has increased by 3.15 Nm, has better overload capacity, and has the characteristics of a reverse salient at low speeds and heavy loads. The constant power speed range can reach up to 4 times of the rated speed, and it has higher efficiency at speeds equal to the rated speed and above 4000 rpm. The power factor is close to 1.0 at high speeds.

In conclusion, the designed VLF-DSPM motor is compared and analyzed with the traditional Delta-type indoor permanent magnet synchronous motor in this paper, and the results are shown in Table 2. Under the premise of ensuring the same stator structure and basically the same number of permanent magnets, the clever design of the motor rotor structure achieves the effect of increasing the output torque, improving the motor efficiency and power factor, and enlarging the range of constant power speed regulation.

ACKNOWLEDGEMENT

This work was supported by National Natural Science Foundation of China Grant No. 52067008, in part by Jiangxi Provincial Key Laboratory of Multidimensional Intelligent Perception and Control under No. 2024SSY03161, and in part by Jiangxi Natural Science Foundation Youth Project under 20242BAB20219.

REFERENCES

[1] Wu, J., X. Zhu, Z. Xiang, D. Fan, L. Quan, and L. Xu, "Robust optimization of a rare-earth-reduced high-torque-density PM motor for electric vehicles based on parameter sensitivity region," *IEEE Transactions on Vehicular Technology*, Vol. 71, No. 10, 10 269–10 279, Oct. 2022.

[2] Monadi, M., M. Nabipour, F. Akbari-Behbahani, and E. Pouresmaeil, "Speed control techniques for permanent magnet synchronous motors in electric vehicle applications towards sustainable energy mobility: A review," *IEEE Access*, Vol. 12, 119 615–119 632, Oct. 2024.

[3] Dianati, B., S. Kahourzade, and A. Mahmoudi, "Optimization of axial-flux induction motors for the application of electric vehicles considering driving cycles," *IEEE Transactions on Energy Conversion*, Vol. 35, No. 3, 1522–1533, Sep. 2020.

[4] Yan, G., H. Liu, N. Han, S. Chen, and D. Yu, "An optimization method for location and capacity determination of charging stations considering spatial and temporal distribution of electric vehicles," *Proceedings of the CSEE*, Vol. 41, No. 18, 6271–6284, Sep. 2021.

[5] Zhang, Z.-R., D. Wang, and W. Hua, "Overview of configuration, design and control technology of hybrid excitation machines," *Proceedings of the CSEE*, Vol. 40, No. 24, 1522–1533, Dec. 2020.

[6] Wang, S., X. Zhang, X. Zhao, S. Niu, and W. Fu, "A novel slot-pm assisted complementary-rotor doubly salient machine with enhanced torque performance," *IEEE Transactions on Industrial Electronics*, Vol. 69, No. 11, 11 499–11 509, Nov. 2022.

[7] Parveen, H. and B. Singh, "Solar photovoltaic fed synchronous reluctance motor with optimized rotor flux barriers: Design and performance optimization," *E-Prime — Advances in Electrical Engineering, Electronics and Energy*, Vol. 9, 100761, Sep. 2024.

[8] Diao, C., W. Zhao, Y. Liu, and X. Wang, "Permanent magnet assisted synchronous reluctance motor with asymmetric rotor for high torque performance," *CES Transactions on Electrical Machines and Systems*, Vol. 7, No. 2, 179–186, Jun. 2023.

[9] Shao, L., D. Tavernini, A. E. H. Karci, and A. Sorniotti, "Design and optimisation of energy-efficient pm-assisted synchronous reluctance machines for electric vehicles," *IET Electric Power Applications*, Vol. 17, No. 6, 788–801, Jun. 2023.

[10] Okamura, M. and T. Takaoka, "The evolution of electric components in prius," *IEEJ Journal of Industry Applications*, Vol. 11, No. 1, 1–6, May 2022.

[11] Gierczynski, M., R. Jakubowski, E. Kupiec, M. Seredynski, M. Jaworski, and L. M. Grzesiak, "Modeling of the fourth-generation toyota prius traction machine as the reference for future designs," *Energies*, Vol. 17, No. 19, 4796, Sep. 2024.

[12] Davarpanah, G., J. Faiz, H. Shirzad, and M. Lotfizadeh, "A modular hybrid excited switched reluctance motor with two groups of permanent magnets to enhance the performance of the motor," *IEEE Transactions on Energy Conversion*, Vol. 39, No. 3, 1686–1698, Sep. 2024.

[13] Wang, H., Y. Xue, J. Du, and H. Li, "Design and evaluation of modular stator hybrid-excitation switched reluctance motor for torque performance improvement," *IEEE Transactions on Industrial Electronics*, Vol. 71, No. 10, 12 814–12 823, Oct. 2024.

[14] Li, N., D. Xu, X. Hao, and J. Li, "Design and analysis of a series-type permanent magnet axial flux-switching memory machine," *Energies*, Vol. 15, No. 23, 8954, Nov. 2022.

[15] Sun, T., X. Liu, Y. Zou, C. Huang, and J. Liang, "Design and optimization of a mechanical variable-leakage-flux interior permanent magnet machine with auxiliary rotatable magnetic poles," *CES Transactions on Electrical Machines and Systems*, Vol. 5, No. 1, 21–29, Mar. 2021.

[16] Xing, Z., X. Wang, W. Zhao, X. Li, L. Xiong, and X. Zhang, "Optimization design of interior permanent magnet synchronous motor with U-shaped rotor for low-level torque ripple and electromagnetic vibration," *IEEE Transactions on Transportation Electrification*, Vol. 10, No. 1, 1995–2007, Mar. 2024.

[17] Wang, H., Z. Hao, X. Li, G. Jiang, and L. Guo, "Reverse salient pole design of interior pole-changing permanent magnet synchronous motor," *Journal of Magnetics*, Vol. 29, No. 1, 77–87, 2024.

[18] Muhammad, N., F. Khan, B. Ullah, S. Tariq, and A. H. Milyani, "Design and analysis of an asymmetric spoke and delta-shape interior permanent magnet synchronous machine," *IEEE Access*, Vol. 11, 54 849–54 858, May 2023.

[19] Zhu, W., X. Liu, G. Guo, and Q. Zhang, "Design and evaluation of a novel controllable leakage flux permanent magnet motor with wide speed ranges," in *2021 IEEE 4th International Electrical and Energy Conference (CIEEC)*, 1–4, Wuhan, China, 2021.

[20] Zhao, X., B. Kou, C. Huang, and L. Zhang, "A reverse-salient permanent magnet synchronous motor for electric vehicles considering operating conditions," *IEEE Transactions on Energy Conversion*, Vol. 38, No. 1, 262–272, Mar. 2023.

[21] Wang, J., X. Zhu, L. Xu, *et al.*, "Research on magnetic field control of leakage flux controllable interior permanent magnet motor based on open winding," *Proceedings of the CSEE*, Vol. 40, No. 4, 1290–1301, May 2021.

[22] Zhu, X., Z. Xiang, L. Quan, W. Wu, and Y. Du, "Multimode optimization design methodology for a flux-controllable stator permanent magnet memory motor considering driving cycles," *IEEE Transactions on Industrial Electronics*, Vol. 65, No. 7, 5353–5366, Jul. 2018.